The Astrophysical Journal, 605:480–492, 2004 April 10

A MODEL FOR DYNAMIC EVOLUTION OF EMERGING MAGNETIC FIELDS IN THE SUN

T. Magara
E. O. Hulburt Center for Space Research, Naval Research Laboratory, Washington, DC 20375-5352; and Space Sciences Laboratory, University of California, 7 Gauss Way, Berkeley, CA 94720-7450; magara@nrl.navy.mil
Received 2003 October 3; accepted 2003 December 18

ABSTRACT

In this paper we study the dynamic evolution of emerging magnetic fields in the solar atmosphere by deriving a model based on a three-dimensional MHD simulation. The simulation shows that magnetic field lines initially forming a twisted flux tube below the solar surface emerge into the atmosphere by magnetic buoyancy. Outer field lines of the flux tube are almost free to expand in a wide fan shape without strong confinement by surrounding field lines. On the other hand, inner field lines are subject to strong confinement by adjacent twisted field lines that prevent the lateral expansion of inner field lines. By examining the result of the simulation, we derive a model of emerging field lines to demonstrate that the height of an emerging field line increases at the average rate of $(g_0\kappa)^{1/2}H/2$, where g_0, κ, and H are the gravitational acceleration, curvature of the emerging field line, and a scale height of magnetic field strength. Applying this model to the outer and inner field lines, we show that inner field lines are less dynamical than outer field lines and inner field lines are likely to form quasi-static structure in the corona such as prominences and sigmoids. We also discuss that the shape of inner field lines is reflected in the chirality of a modeled sigmoid.

Subject headings: methods: numerical — MHD — Sun: corona — Sun: magnetic fields — Sun: prominences

1. INTRODUCTION

Since the discovery of a close relation between emerging magnetic fields and active phenomena observed in the solar atmosphere, much attention has been given to the dynamical behavior of emerging magnetic fields that originally come from below the solar surface by magnetic buoyancy (Parker 1955). This process, called magnetic flux emergence, is a fundamental process for solar activity in the sense that it brings magnetic fields into the solar atmosphere where they provide energy sources for various activities. So far, a considerable number of observational studies have been made to show that flux emergence is a highly dynamic process in which the magnetic field rapidly changes its state when emerging from a dense subsurface region into a rarefied atmosphere.

From a theoretical point of view, a feasible way of modeling flux emergence is to use the numerical simulation that reproduces the dynamic behavior of emerging magnetic fields. Over the last decade, a number of works have been devoted to performing two- or three-dimensional numerical simulations of flux emergence. Shibata et al. (1989) used two-dimensional MHD simulations to investigate how a subphotospheric magnetic sheet expands into the corona. Their simulations fit an analytic solution for the nonlinear phase of the Parker (i.e., *buoyancy*) instability found by assuming the self-similarity of expansion (Shibata, Tajima, & Matsumoto 1990; Tajima & Shibata 1997, p. 189). Similar two-dimensional studies have been made to demonstrate the convective-Parker instability of an expanding magnetic loop (Nozawa et al. 1992), the interaction between emerging magnetic fields and coronal magnetic fields (Yokoyama & Shibata 1996), and the expansion of emerging magnetic fields in flux tube geometry (Krall et al. 1998; Magara 2001). Matsumoto et al. (1993) extended two-dimensional studies by performing three-dimensional simulations of an emerging magnetic sheet and studied the coupled effect of the interchange mode and the undular mode developed in the magnetic sheet. Later, Matsumoto et al. (1998) and Magara & Longcope (2001) showed that an emerging flux tube assumes sigmoidal structure in the corona, while Fan (2001) discussed the photospheric flow driven by an emerging flux tube. Very recently, Magara & Longcope (2003, hereafter Paper I) calculated the amount of magnetic energy and magnetic helicity injected into the atmosphere by an emerging flux tube, and Fan & Gibson (2003) demonstrated that a twisted flux tube emerging into a preexisting coronal arcade becomes kink unstable, forming an S-shaped current layer. In addition, Abbett & Fisher (2003) studied the structure of a twisted flux tube before and after it emerges into the atmosphere and concluded that a less twisted flux tube forms more potential-like structure in the corona.

Those numerical simulations, especially three-dimensional simulations, have so far provided many fruitful results that help us understand the dynamics of emerging magnetic fields. For example, Paper I showed that outer field lines of an emerging flux tube evolve differently from inner field lines. The aim of the present study is to investigate in further detail the dynamic evolution of the outer and inner field lines. To this end, we first perform a three-dimensional MHD simulation and then derive a simulation-based model for dynamic evolution of emerging field lines, which is used to study how the shape of emerging field lines affects their evolution. We also discuss the structure formed by emerging field lines with emphasis on the chirality of structure.

The next section describes an MHD numerical simulation, and § 3 shows the result obtained by the simulation. In § 4 we explain how we derive a model of emerging field lines and then discuss the relation between the shape and evolution of emerging field lines. In § 5 we consider the chirality of

emerging field lines that have sigmoidal structure. The final section presents a summary of this study.

2. NUMERICAL SIMULATION

2.1. *Basic Equations and a Numerical Method*

We use a standard set of ideal MHD equations including a uniform gravity. These equations are written by

$$\frac{\partial \rho}{\partial t} + \nabla \cdot (\rho \boldsymbol{v}) = 0, \tag{1}$$

$$\rho \left[\frac{\partial \boldsymbol{v}}{\partial t} + (\boldsymbol{v} \cdot \nabla) \boldsymbol{v} \right] = -\nabla P + \frac{1}{4\pi} (\nabla \times \boldsymbol{B}) \times \boldsymbol{B} + \rho \boldsymbol{g}_0, \tag{2}$$

$$\frac{\partial \boldsymbol{B}}{\partial t} = \nabla \times (\boldsymbol{v} \times \boldsymbol{B}), \tag{3}$$

$$\frac{\partial P}{\partial t} + \nabla \cdot (P \boldsymbol{v}) = -(\gamma - 1) P \nabla \cdot \boldsymbol{v}, \tag{4}$$

and

$$P = \frac{\rho \Re T}{\mu}, \tag{5}$$

where ρ, $\boldsymbol{v}$, $\boldsymbol{B}$, P, $\boldsymbol{g}_0$, γ, μ, $\Re$, and T indicate the gas density, fluid velocity, magnetic field, gas pressure, gravitational acceleration, adiabatic index ($\gamma = \frac{5}{3}$ is assumed), mean molecular weight ($\mu = 0.6$ is assumed), gas constant, and temperature, respectively. The numerical method for solving those equations is a modified Lax-Wendroff scheme that has second-order accuracy in both time and space (Magara 1998). The simulation box is $(-100,\ -100,\ -10) \le (x, y, z) \le (100,\ 100,\ 100)$, where x and y are horizontal coordinates and z is a vertical coordinate. The basic equations (1)–(4) are discretized on a nonuniform Cartesian grid. The grid spacing increases from $(\Delta x, \Delta y, \Delta z) = (0.2,\ 0.4,\ 0.2)$ toward (4, 4, 4), and the finest grid occupies the region of $(-8,\ -12,\ -10) \le (x, y, z) \le (8,\ 12,\ 10)$. The total grid number is $N_x \times N_y \times N_z = 215 \times 167 \times 168$.

2.2. *Initial Conditions*

The initial state is identical to the one presented in Paper I, a magnetohydrostatic state in which a magnetic flux tube is placed in a stratified atmosphere extending from the subphotosphere to the corona. The unit of length and velocity is given by $2H_p$ and c_{sp}, where H_p and c_{sp} are the pressure scale height and the adiabatic sound speed at the photosphere. They are defined as $H_p = \Re T_p/(\mu g_p) = 2.7 \times 10^7$ cm and $c_{sp} = (\gamma \Re T_p/\mu)^{1/2} = 11$ km s^{-1}, where $T_p = 5100$ K is the temperature at the photosphere (used as the unit of temperature) and $g_p = 274$ m s^{-2} is the gravitational acceleration at the solar surface. Accordingly, the unit of time and acceleration is given by $2H_p/c_{sp} = 49$ s and $c_{sp}^2/(2H_p) = (\gamma/2) g_p = 228$ m s^{-2}, so the dimensionless gravitational acceleration at the solar surface is $g_0 = 2/\gamma$. In addition, $\gamma P_p = 3.33 \times 10^5$ dyn cm^{-2}, $\rho_p = 2.7 \times 10^{-7}$ g cm^{-3}, and $(\gamma P_p)^{1/2} = 570$ G are the unit of gas pressure, gas density, and magnetic field, where P_p and ρ_p are the gas pressure and gas density at the photosphere, respectively.

Using those units, we then define the initial distribution of temperature, gas pressure, gas density, and magnetic field in dimensionless form. The distribution of temperature depends on the vertical coordinate alone, which is given by

$$T(z) = \begin{cases} T_0 - S_a \left| \dfrac{dT}{dz} \right|_{\rm ad} \left(\dfrac{1}{4} \ln \left\{ \dfrac{\cosh(2z_{\rm ph})}{\cosh[2(z - z_{\rm ph})]} \right\} + \dfrac{z}{2} \right), & z_{\rm cv} \le z < z_{\rm ph}, \\ T_0 + (T_1 - T_0) \left\{ \dfrac{1}{2} \left[\tanh\left(\dfrac{z - z_{\rm tr}}{w_{\rm tr}} \right) + 1 \right] \right\}, & z_{\rm ph} \le z < z_{\rm tr}, \\ \left(T_0 + (T_1 - T_0) \left\{ \dfrac{1}{2} \left[\tanh\left(\dfrac{z - z_{\rm tr}}{w_{\rm tr}} \right) + 1 \right] \right\} \right) & \\ \quad \times \left(\dfrac{z - z_{\rm tr}}{z_{\rm cr} - z_{\rm tr}} + 1 \right), & z_{\rm tr} \le z < z_{\rm cr}, \\ 2 \left(T_0 + (T_1 - T_0) \left\{ \dfrac{1}{2} \left[\tanh\left(\dfrac{z - z_{\rm tr}}{w_{\rm tr}} \right) + 1 \right] \right\} \right), & z_{\rm cr} \le z, \end{cases} \tag{6}$$

where $S_a = 1.025$, $|dT/dz|_{\rm ad} \equiv (\gamma - 1) g_0 = 0.4$, $T_0 = 1$, $T_1 = 100$, $z_{\rm cv} = -8$, $z_{\rm ph} = 0$, $z_{\rm tr} = 7.5$, $z_{\rm cr} = 20$, and $w_{\rm tr} = 0.5$. This temperature profile defines four atmospheric layers: the subphotosphere ($z < z_{\rm ph}$), the photosphere and chromosphere ($z_{\rm ph} < z < z_{\rm tr}$), the transition region ($z \sim z_{\rm tr}$), and the corona ($z > z_{\rm tr}$). In the subphotosphere the gradient of temperature takes a slightly superadiabatic value ($S_a > 1$), so this region is convectively unstable. Using equation (6), we define the distribution of gas pressure and gas density as

$$P(z) = P_0 \exp\left[-\int_{z_{\rm ph}}^{z} \frac{\gamma g_0}{T(z')}\, dz' \right] \tag{7}$$

and

$$\rho(z) = \frac{\gamma P(z)}{T(z)}, \tag{8}$$

where we take $P_0 = 1/\gamma$ as the photospheric gas pressure.

The magnetic field initially forms a flux tube with a left-handed twist below the photosphere. The distribution of magnetic field inside the flux tube is given by

$$\boldsymbol{B} = B_0 \frac{-b(z - z_0)\hat{x} + \hat{y} + b(x - x_0)\hat{z}}{1 + b^2 \left[(x - x_0)^2 + (z - z_0)^2 \right]} \tag{9}$$

$[(x - x_0)^2 + (z - z_0)^2 < r_0^2]$, where $(x_0, z_0) = (0,\ -4)$, $b = 1$, $r_0 = 2$, and $B_0 = 17.4$. This is a force-free straight flux tube whose axis is parallel to the y-axis. Inside the flux tube, the gas pressure is given by

$$P_{\rm tube}(z) = P(z) - \frac{B_0^2}{8\pi} \frac{1}{b^2 r_0^2 + 1}, \tag{10}$$

where $P_{\rm tube}(z)$ is the gas pressure inside the flux tube and $P(z)$ is given by equation (7). Equation (10) indicates that the gradient of gas pressure in the z-direction has the same value between inside and outside the flux tube. Hydrostatic equilibrium requires that the gas density inside the flux tube is also the same as outside, while the temperature inside the flux tube is lower than outside. Figure 1 shows the initial configuration of the simulation.

2.3. *Imposed Motion*

In order to initiate the emergence of the magnetic flux tube given by equation (9), we impose an artificial motion that

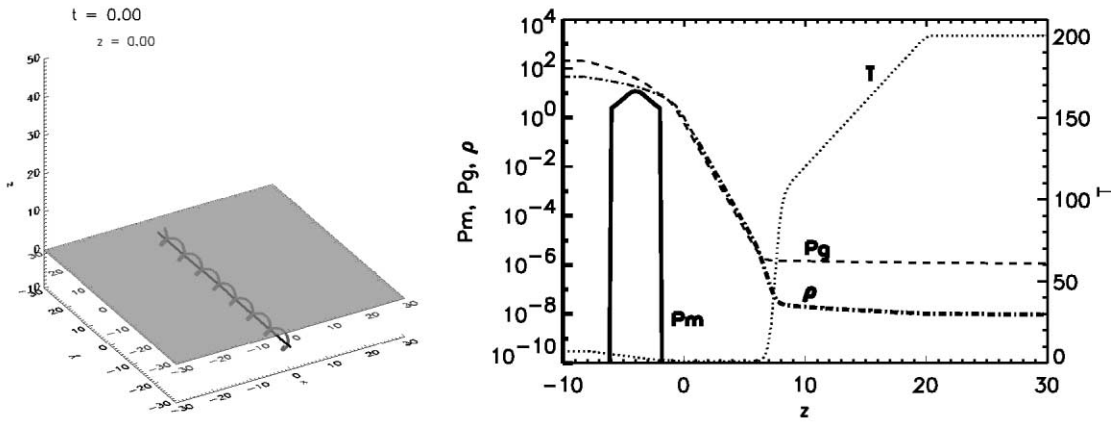

FIG. 1.—*Left*: Initial state of the simulation. Gray and black lines represent an outer and inner field line, respectively, of a magnetic flux tube located below the photosphere. A horizontal gray-scale map represents the photospheric plane. *Right*: Initial distribution of physical quantities along the z-axis, such as the gas pressure (P_g), density (ρ), temperature (T), and magnetic pressure provided by a magnetic flux tube (P_m). Temperature is plotted linearly against the right axis, and the other quantities are plotted logarithmically against the left axis.

forces the flux tube to undulate along the axis. The motion is driven by applying a time-dependent vertical velocity field during $0 < t < t_0$:

$$v_z(x, y, z, t) = v_0 \cos\left(2\pi \frac{y}{\lambda}\right) \sin\left(\frac{\pi}{2} \frac{t}{t_0}\right) \qquad (11)$$

$[(x - x_0)^2 + (z - z_0)^2 < r_0^2,\ -\frac{3}{4}\lambda \le y \le \frac{3}{4}\lambda]$, where $t_0 = 5$, $v_0 = 0.16$, and $\lambda = 20$, while x_0, z_0, and r_0 are given above in equation (9). A downflow then arises inside an undulating flux tube, inducing magnetic buoyancy that pushes the Ω part of the flux tube toward the origin at the photospheric plane where fine grids are distributed.

2.4. *Boundary Conditions*

The initial condition and the imposed motion described above are symmetric with respect to 180° rotation about the z-axis accompanied by a reflection of the magnetic field vector. Under this operation, B_z, v_x, and v_y change sign while all other quantities are unchanged. We take advantage of this symmetry to advance only one-half of the simulation domain, $(0, -100, -10) \le (x, y, z) \le (100, 100, 100)$, and provide a symmetric boundary condition at the $x = 0$ plane. We impose periodic boundary conditions at $y = \pm 100$, a free boundary condition at $x = 100$ and $z = 100$, and a fixed, impermeable boundary condition at $z = -10$ (the initial value of each physical quantity is held fixed). In addition, we place a nonstratified isothermal layer (zero-gravity layer) near the top and bottom boundaries, as well as a wave-damping region near all the boundaries except for $x = 0$.

3. SIMULATION RESULT

In Paper I we showed that each field line of an emerging flux tube evolves differently depending on the position inside the flux tube. Outer field lines apart from the axis of the flux tube emerge first into the photosphere and continue to expand into the corona. On the other hand, inner field lines near the tube axis emerge later into the photosphere, and they do not simply continue to expand but stay near the photosphere at least temporarily. Here we study the subsequent phase during which inner field lines expand into the corona. In order to accelerate the evolution of inner field lines, we impose an undular motion with a relatively short wavelength ($\lambda = 20$ in the present study compared to $\lambda = 30$ in Paper I). In this case the axis of the flux tube undulates so tightly that plasma inside the flux tube drains efficiently, whereby enhanced magnetic buoyancy quickly brings inner field lines to the corona.

Figure 2 shows snapshots taken at $t = 36$ of an outer field line (*gray line*) and an inner field line (*black line*) that originally corresponds with the axis of the flux tube (see Fig. 1). After emerging, the outer field line spreads out in a wide fan, while the inner field line extends mainly in the vertical direction. The situation is more obvious in Figure 3, where we display the distribution of gas density (*colors*) and velocity field (*arrows*) on the outer and inner field line. A density-reduced area lies in the fan-shaped part of the outer field line, and the velocity field in this area suggests that the outer field line continues to expand, keeping the fan shape. Similar density reduction can be observed in the upper part of the inner field line where vertical motions are dominant.

The way of expansion of the outer and inner field line is related to how these field lines are surrounded by adjacent field lines. Figure 4 shows snapshots of the same outer and inner field line as in Figures 2 and 3, although the snapshots in Figure 4 are taken at $t = 40$ together with other field lines forming the flux tube (*light gray lines*). An examination of the spatial relations of those field lines shows that the inner field line is tightly surrounded by adjacent twisted field lines, especially along both of its legs. Such confinement by surrounding field lines prevents the lateral expansion of the inner field line. On the other hand, the outer field line is almost free to expand without strong confinement by surrounding field lines. Consequently, the outer and inner field lines have a different shape while they are expanding into the corona: the outer field line forms a widely spread fanlike structure in the corona with a small footpoint distance at the photosphere, while the inner field line extending from the photosphere to the corona tends to keep the same footpoint distance.

4. A SIMULATION-BASED MODEL OF EMERGING FIELD LINES

In this section we introduce a model for dynamic evolution of emerging field lines. In this model, we discuss the time

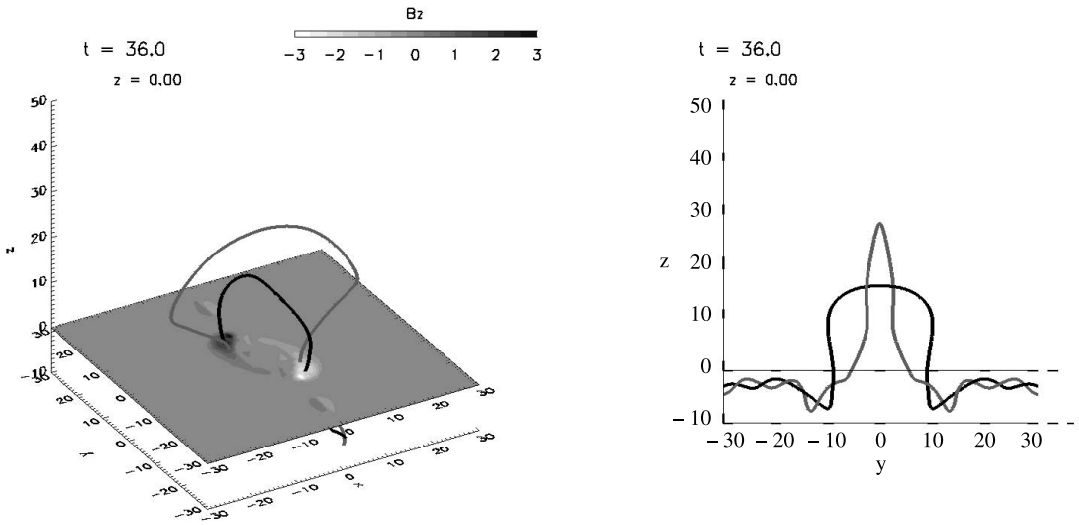

FIG. 2.—Snapshots of an outer (*gray line*) and inner (*black line*) field line taken at $t = 36$, showing the perspective view (*left*) and side view (*right*). A gray-scale map shows the vertical magnetic flux at the photosphere.

history of a plasma element in the middle of an emerging field line. Our approach is to solve the momentum equation under a prescribed distribution of the magnetic field obtained by the simulation shown in the previous section. Compared to more general approaches such as solving the induction equation, the present approach focuses on the plasma motion affected by the magnetic field in a magnetically strong region such as the solar corona. We first derive an evolution equation that describes how the plasma element evolves along the symmetric axis of an emerging field line. Then we solve the equation to investigate the relation between the shape and evolution of emerging field lines.

4.1. *An Evolution Equation*

Figure 5*a* schematically illustrates an emerging field line (*thick black line*) and three forces exerted on a plasma element in the middle of the field line (*arrows*). We here assume the same spatial symmetry as in the simulation, so the plasma element always moves along the z-axis and all the forces exerted on this element point in the vertical direction. We furthermore assume that the magnetic pressure force, magnetic tension force, and gravitational force are the dominant forces affecting plasma. The gas pressure force is sufficiently weak compared to those three forces except for near the photosphere (see Figs. 4 and 6 in Paper I).

The momentum equation in the middle of the field line is given by

$$\rho \frac{d^2 Z(t)}{dt^2} = F_M + F_T + F_G, \tag{12}$$

where ρ and $Z(t)$ are the gas density and height of the plasma element, while F_M, F_T, and F_G represent the magnetic pressure force, magnetic tension force, and gravitational force. In the present study we confine our attention to the case that the emerging field line always has an Ω shape. Accordingly, F_T is always negative and F_G is also negative. F_M takes either a positive or negative value, and we later define the sign of F_M using the simulation.

The gas density in the middle of the field line is determined by the continuum equation:

$$\frac{d\rho}{dt} = -\rho \frac{\partial v_s}{\partial s}, \tag{13}$$

where ds is the infinitesimal length of the field line and v_s is the field-aligned velocity. This is an approximate equation because it assumes that the vertical expansion and contraction of plasma are less important than the lateral expansion and contraction. The simulation shows that when a field line enters on a phase of continuous expansion, lateral expansion is dominant in the middle of the field line even though there is a large vertical velocity because oppositely directed v_s naturally gives rise to lateral expansion while large but almost uniform v_z produces small net vertical expansion (see Fig. 5*b*). We hence proceed with equation (13) in the present study, which gives us the time history of gas density expressed in terms of the curvature in the middle of the field line:

$$\rho(t) = \rho_i \exp\left(-\int_0^t \sqrt{g_0 \kappa}\, dt'\right), \tag{14}$$

where $\rho = \rho_i$ at $t = 0$, while g_0 is the gravitational acceleration and κ is the curvature. When we derived equation (14), we used $v_s \sim (g_0 \kappa)^{1/2} s$, which is obtained from a free-fall equation along the field line:

$$\frac{dv_s}{dt} = g_0 \sin\theta \sim g_0 \kappa s \quad \text{for } \theta \ll 1, \tag{15}$$

where $v_s \equiv ds/dt$, θ is an angle from the z-axis, and s is a signed length taking a positive sign toward the right from the middle of the field line and a negative sign toward the left (see Fig. 5*b*). We again neglect the gas pressure force in equation (15).

The three forces on the right-hand side of equation (12) are expressed as

$$F_M = -\frac{\partial}{\partial z}\left(\frac{B^2}{8\pi}\right), \tag{16}$$

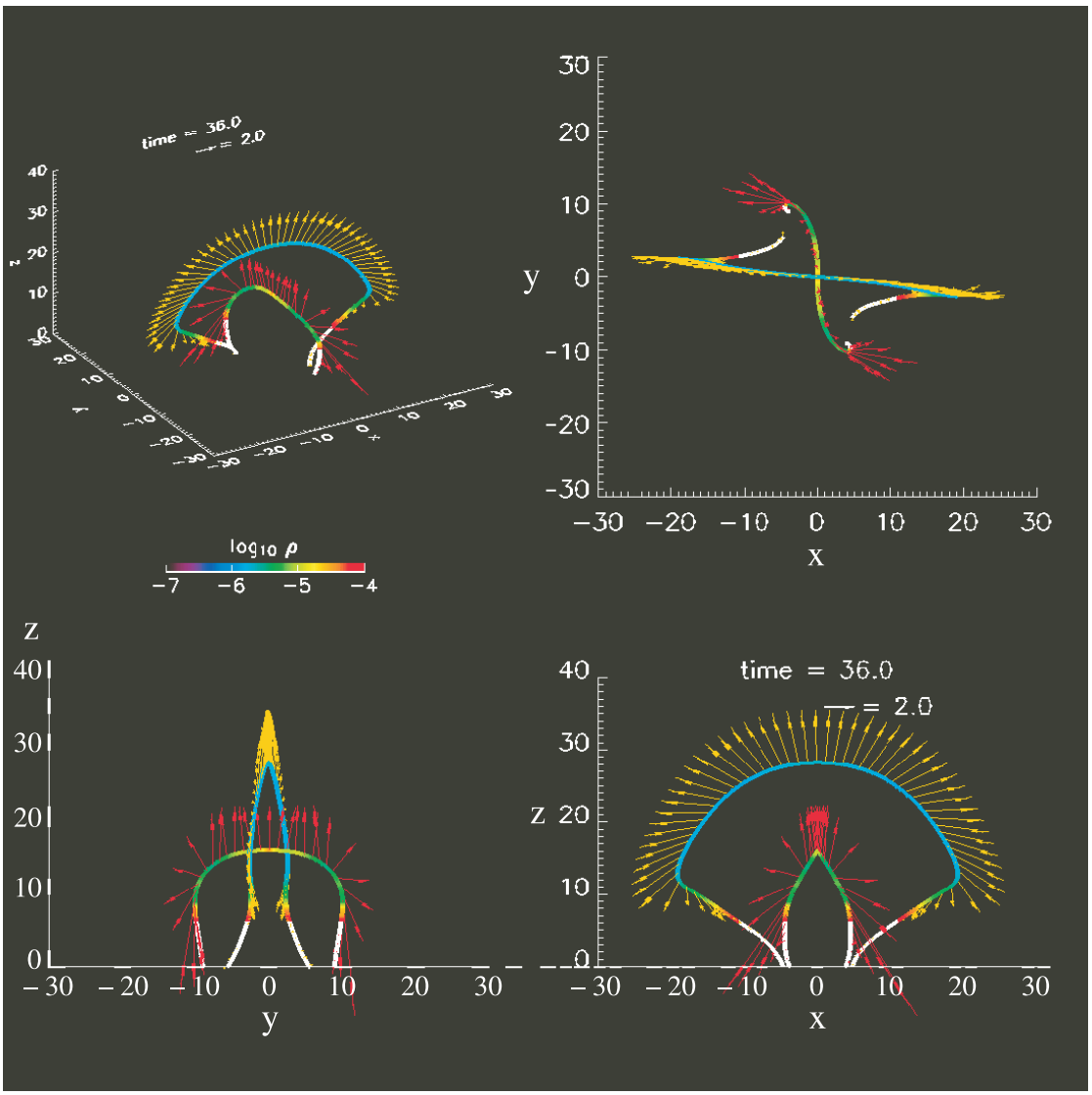

FIG. 3.—Four snapshots (top, side, front, perspective views) of an outer and inner field line taken at $t = 36$. Arrows and colors show the velocity field and gas density on those field lines. White is the color in excess of red in the color scale, indicating high density.

$$F_T = -\frac{B^2}{4\pi}\kappa, \tag{17}$$

and

$$F_G = -\rho g_0, \tag{18}$$

where ρ is given by equation (14). We now refer to the simulation to see the distribution of magnetic field strength along the z-axis. In Figure 6 we plot the relation of (z, B) at $t = 32$, 34, 36, 38, and 40. According to these plots, we approximate that the magnetic field strength has the same z dependence at each time, which is expressed by

$$B(x = 0,\ y = 0,\ z, t) = B_i \exp\left(-\frac{z - z_i}{H}\right), \tag{19}$$

where $B = B_i$ at $z = z_i$, while H is a typical scale height of magnetic field strength, which is assumed to be constant in time and space. We use this approximate relation to obtain the temporal development of plasma motion under the prescribed magnetic field, which is then compared to the result obtained by the full MHD simulation. Using equation (19), we rewrite equations (16) and (17) as

$$F_M = \frac{1}{H}\frac{B_i^2}{4\pi}\exp\left[-2\frac{Z(t) - z_i}{H}\right] \tag{20}$$

and

$$F_T = -\kappa\frac{B_i^2}{4\pi}\exp\left[-2\frac{Z(t) - z_i}{H}\right]. \tag{21}$$

Equation (20) indicates that the magnetic pressure force always goes upward. Substituting equations (14), (18), (20), and (21) into equation (12), we finally obtain an evolution equation about the height of an emerging field line:

$$\ddot{Z}(t) = \left(\frac{1}{H} - \kappa\right)\frac{B_i^2}{4\pi\rho_i}\exp\left[-2\frac{Z(t) - z_i}{H} + \int_0^t \sqrt{g_0\kappa}\, dt'\right] - g_0, \tag{22}$$

where $\ddot{Z}(t) \equiv d^2Z/dt^2$.

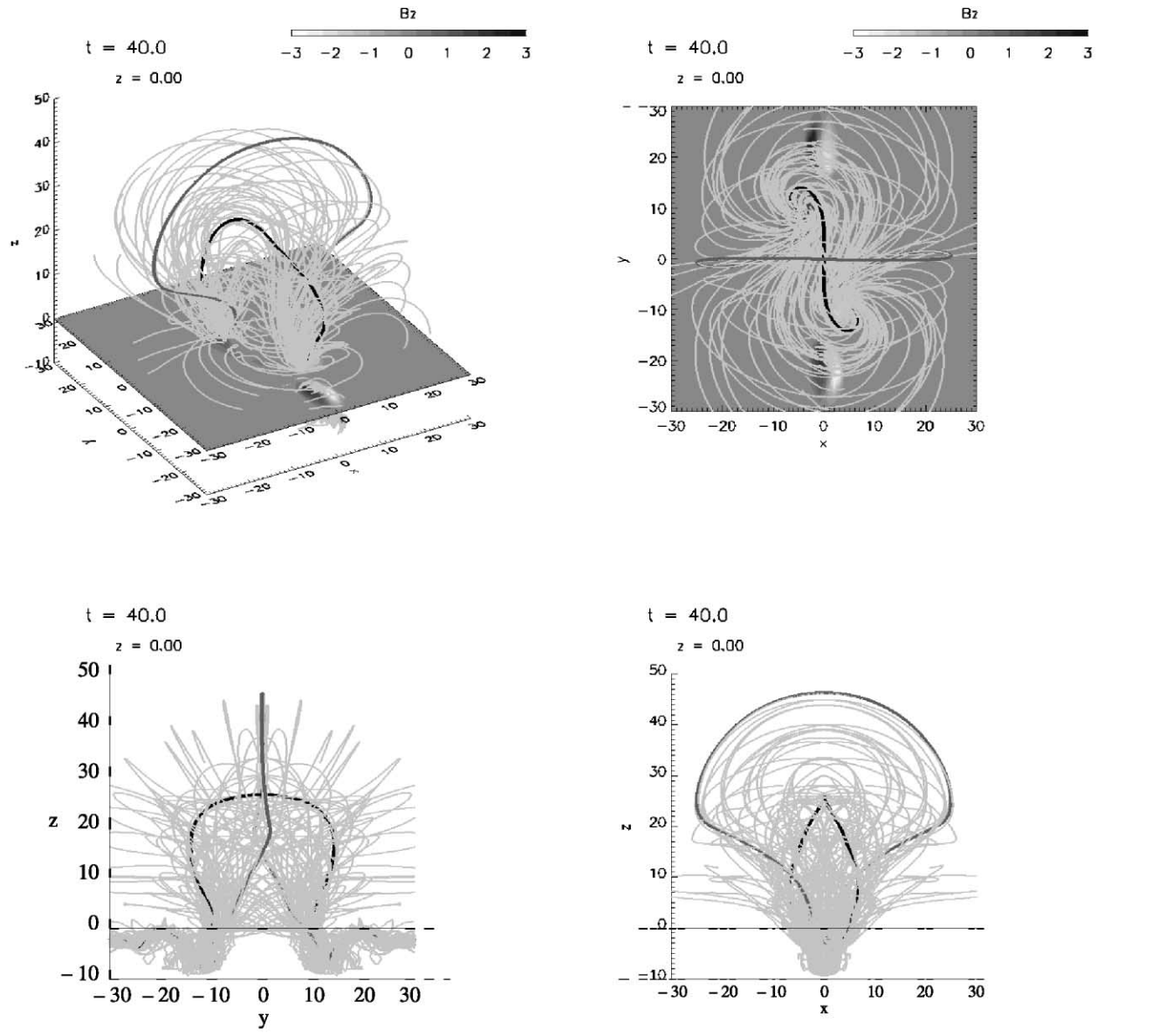

FIG. 4.—Four snapshots (top, side, front, perspective views) of an outer (*gray line*) and inner (*black line*) field line taken at $t = 40$ together with other field lines forming a flux tube (*light gray lines*). A gray-scale map shows the vertical magnetic flux at the photosphere.

4.2. *Comparison to Simulation*

In this section we compare the result obtained by solving equation (22) with the result obtained by an MHD simulation. First, we define the initial condition of equation (22). Taking $Z(0) = z_i$ and $\dot{Z}(0) = 0$ [$\dot{Z}(t) = dZ/dt$], we assume that all the forces initially balance each other. The force balance equation is written by

$$0 = \left(\frac{1}{H} - \kappa\right)\frac{B_i^2}{4\pi\rho_i} - g_0. \tag{23}$$

According to equation (23), $1/H > \kappa$ is required for force balance. Taking $z_i = 0$ for the present study, we then rewrite equations (22) and (23) as follows:

$$\ddot{Z}(t) = \left(\frac{1}{H} - \kappa\right)v_{\mathrm{A}i}^2 \exp\left[-2\frac{Z(t)}{H} + \int_0^t \sqrt{g_0\kappa}\, dt'\right] - g_0 \tag{24}$$

and

$$v_{\mathrm{A}i}^2 = g_0\left(\frac{1}{H} - \kappa\right)^{-1}, \tag{25}$$

where $v_{\mathrm{A}i} \equiv B_i/(4\pi\rho_i)^{1/2}$.

Next, we refer to the simulation to determine κ and H. The simulation shows that the outer field line tends to keep almost the same curvature in the middle of the field line when it enters on a phase of continuous expansion. We find the curvature of the outer field line to be $\kappa = 0.04$, along with $H = 12$ and $B_i = 0.13$, which are obtained by fitting the plots in Figure 6. These H and κ determine $v_{\mathrm{A}i} = 5.3$ according to equation (25). We substitute those H, κ, and $v_{\mathrm{A}i}$ into equation (24), which is then numerically integrated using the fourth-order Runge-Kutta method. The obtained time history of $Z(t)$, $\dot{Z}(t)$, and three forces $F_M(t)$, $F_T(t)$, and $F_G(t)$ is shown in Figure 7*a*.

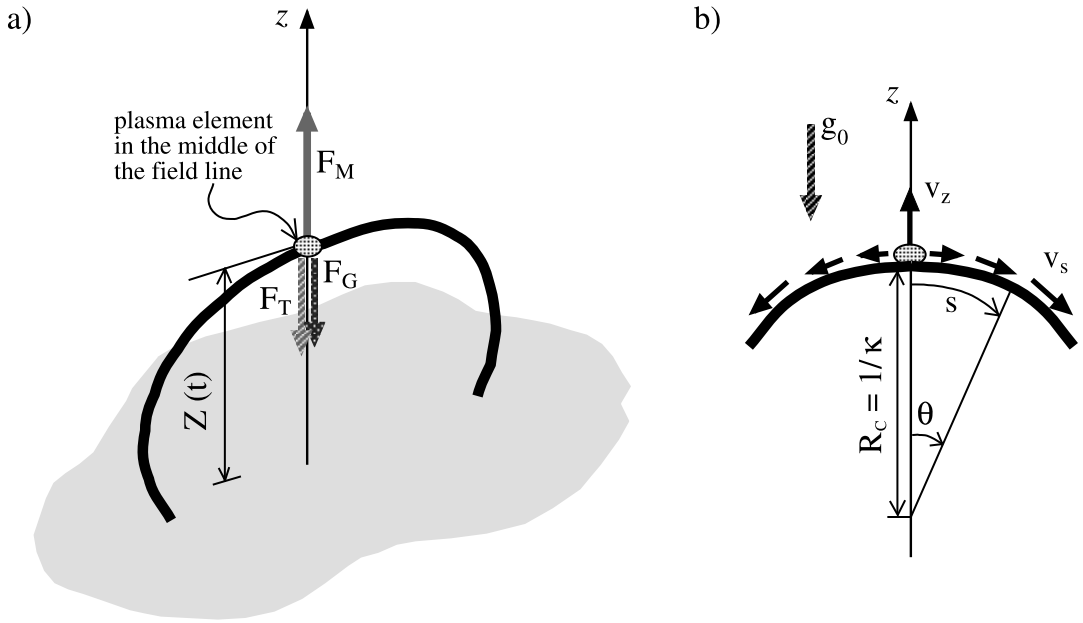

FIG. 5.—(*a*) Schematic viewgraph of an Ω-shaped emerging field line and three forces exerted on a plasma element in the middle of the field line. Here F_M, F_T, and F_G represent the magnetic pressure force, magnetic tension force, and gravitational force. (*b*) Close-up of the middle of the field line. The v_z and v_s represent the vertical velocity and field-aligned velocity, while R_c and κ represent the curvature radius and curvature in the middle of the field line.

A noted feature found in Figure 7*a* is the oscillatory behavior of an emerging field line. From a qualitative viewpoint, this oscillatory behavior can be explained by the coupled effect of the magnetic force and gravitational force. At the beginning, plasma starts to drain from the middle of the field line, and this drives magnetic buoyancy, so $\dot{Z}(t)$ and $Z(t)$ increase with time. At this stage the magnetic effect represented by the first term on the right-hand side of equation (24) is larger than the gravitational effect represented by the second term. Then as $Z(t)$ increases, the magnetic effect becomes weak because the magnetic field strength decreases with height according to equation (19). The gravitational effect therefore dominates the magnetic effect, which causes negative acceleration, and $\dot{Z}(t)$ decreases until the drain of plasma makes the magnetic effect dominant again. In the Appendix we present a quantitative analysis of equation (24) to calculate an approximate value of the period of the oscillatory behavior $\langle T \rangle$, as well as the average velocity $\langle \dot{Z}(t) \rangle$. The result is

$$\langle T \rangle = \pi \sqrt{\frac{2H}{g_0}} \tag{26}$$

and

$$\langle \dot{Z}(t) \rangle = \frac{H}{2} \sqrt{g_0 \kappa}. \tag{27}$$

In the present case, $\langle T \rangle = 14$ and $\langle \dot{Z}(t) \rangle = 1.3$ with $H = 12$, $g_0 = 1.2$ ($g_0 = 2/\gamma$), and $\kappa = 0.04$. The time history of the average height and velocity is also plotted in Figure 7*a*.

Figure 7*b* shows the time history of the outer field line found in the simulation. Here we observe the up-and-down behavior of rising velocity, which is similar to the behavior of $\dot{Z}(t)$ (compare the phase of $12 < t < 27$ in Fig. 7*a* with the phase of $30 < t < 45$ in Fig. 7*b*). The period of this up-and-down behavior is about 15, which is also close to $\langle T \rangle = 14$ given by equation (26). On the other hand, we do not find clear similarity in the time history of force between the model and simulation. Since the grid resolution in the simulation box becomes worse as z is larger ($\Delta z \sim 2$ at $z = 50$ compared to $\Delta z \sim 0.7$ at $z = 20$), physical quantities related to a spatial derivative such as magnetic pressure force and magnetic tension force become less accurate at larger z. The better comparison between the model and simulation will be possible when we perform more advanced numerical simulations in high grid resolution.

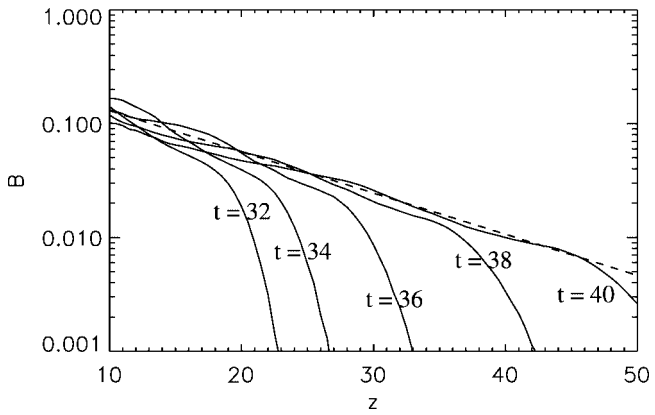

FIG. 6.—Distribution of magnetic field strength along the z-axis at $t = 32$, 34, 36, 38, and 40. A thick dashed line shows the z dependence given by eq. (19) with $B_i = 0.13$, $z_i = 10$, and $H = 12$.

4.3. *Dynamic Evolution Characterized by the Shape of Emerging Field Lines*

Using the model explained above, we now investigate the relation between the shape and evolution of emerging field

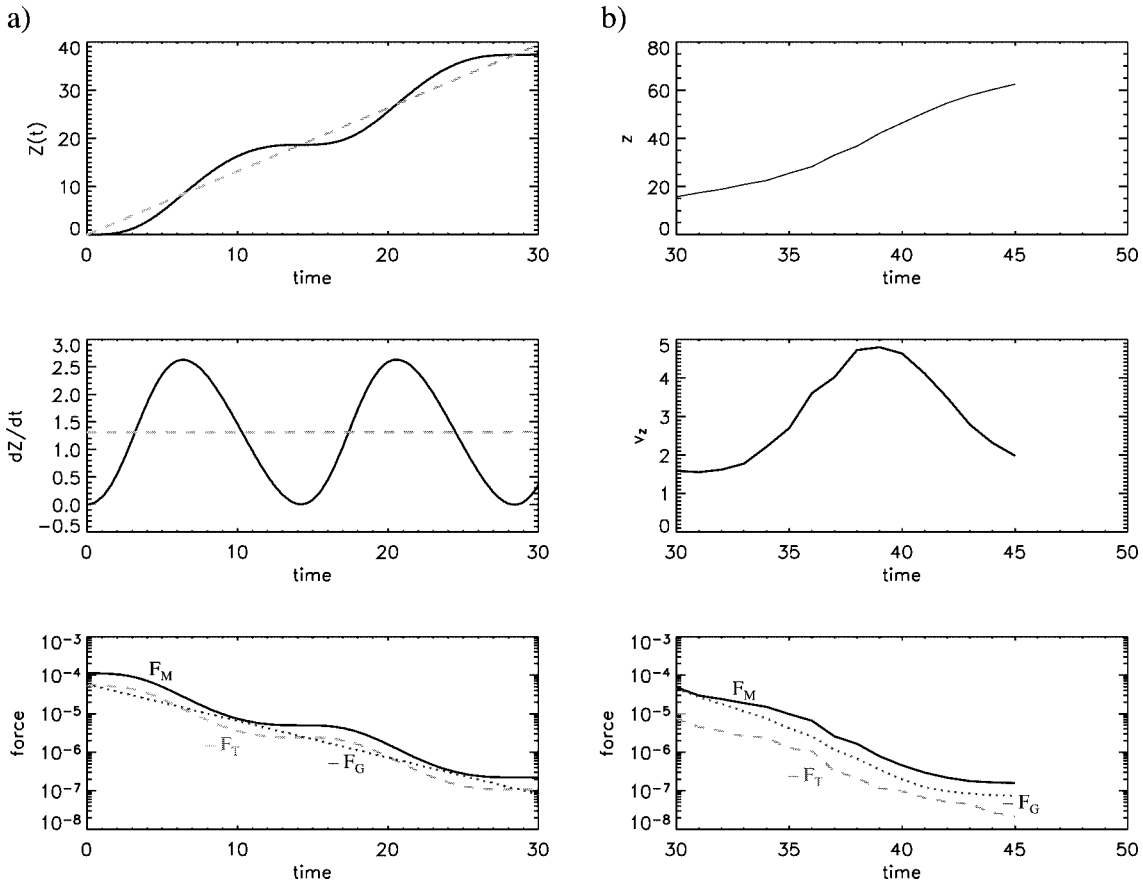

FIG. 7.—(*a*) Time history of the height (*top*), velocity (*middle*), and force (*bottom*) derived from a simulation-based model. In the top and middle panels, the average height and velocity calculated using eq. (27) are shown by a dashed line. In the bottom panel, the magnetic pressure force (*solid line*), magnetic tension force (*dashed line*), and gravitational force (*dotted line*) are displayed. (*b*) Time history of the height (*top*), velocity (*middle*), and force (*bottom*) of the outer field line obtained by the simulation. In the bottom panel, the magnetic pressure force (*solid line*), magnetic tension force (*dashed line*), and gravitational force (*dotted line*) are displayed.

lines. Here we do not discuss realistic evolution of emerging field lines; instead, we focus our attention on the geometrical factor that affects dynamic evolution, especially on the curvature of emerging field lines. Figures 8*a*–8*c* illustrate three types of emerging field lines, each of which has a different pattern of evolution. In Figure 8*a*, a field line spreads out widely, keeping a fan shape during expansion, which reflects the character of the outer field line in the simulation (called type A). Figure 8*b* presents a model of the inner field line in the simulation, which extends mainly in the vertical direction (called type B). In Figure 8*c* a multilobed field line initially forms above the surface, which later changes to a flatter, single-lobed field line by magnetic reconnection between neighboring lobes (called type C). When we focus on the temporal development of the curvature in the middle of a field line, the type A field line almost keeps the same curvature, while the type B field line increases the curvature with time and the type C field line decreases it with time. In order to study how the curvature affects the dynamic evolution of an emerging field line, we express the curvature as a function of time, which is substituted into equation (24). Then we solve the equation and derive the time history for each type of field line.

For the type A field line, we substitute $\kappa = 0.00571$ (constant), $H = 70$, and $v_{Ai} = 11.8$ (calculated from H and κ using eq. [25]) into equation (24). We also use $B_i = 0.13$ to calculate the gas density. Figure 9*a* shows the time history of height, velocity, force, and gas density, in which we observe the field

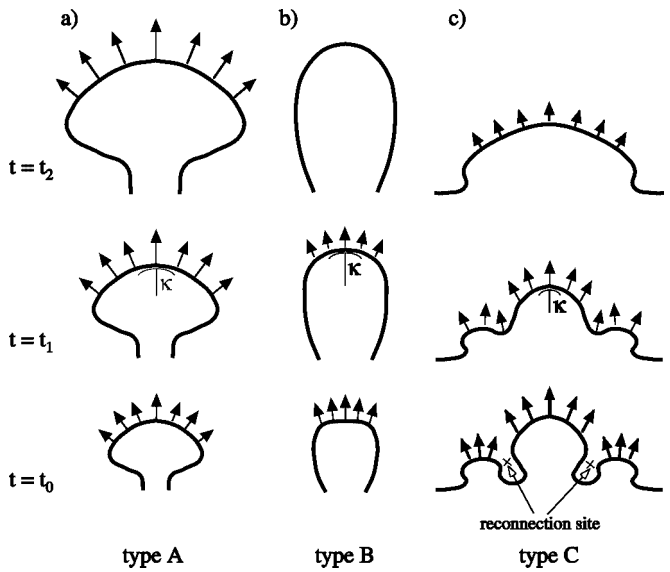

FIG. 8.—Schematic viewgraph of three types of emerging field lines that evolve from $t = t_0$ to $t = t_2$. (*a*) Type A field line continues to expand in a fan shape. (*b*) Type B field line extends mainly in the vertical direction. (*c*) Type C field line forms a multilobed shape above the surface, which is later changed to a single-lobed shape by magnetic reconnection between neighboring lobes.

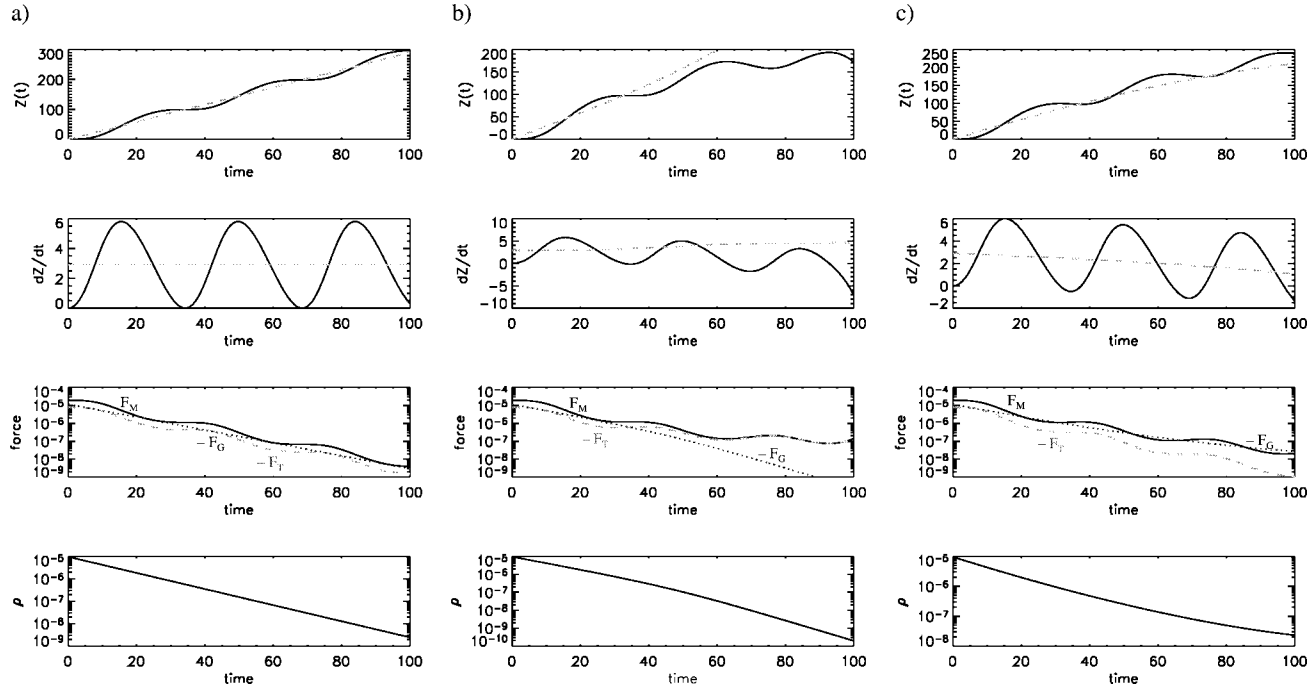

FIG. 9.—(*a*) Time history of the height (*top*), velocity (*second from the top*), force (*third from the top*), and gas density (*bottom*) of the type A field line. In the panel for height and velocity, the average height and velocity calculated using eq. (27) are shown by a dashed line. In the panel for force, the magnetic pressure force (*solid line*), magnetic tension force (*dashed line*), and gravitational force (*dotted line*) are displayed. (*b*) Same as (*a*), but for the type B field line. (*c*) Same as (*a*), but for the type C field line.

line continuously expanding at an up-and-down rate of climb. This is basically the same behavior that the outer field line shows in the simulation.

For the type B field line, we use a time-dependent curvature given by

$$\kappa(t) = (\kappa_1 - \kappa_0)\left\{\frac{\tanh\ [(t-50)/20] + 1}{2}\right\} + \kappa_0, \quad (28)$$

along with the same H, v_{Ai}, and B_i that are taken for the type A field line. Equation (28) indicates that κ temporally increases from $\kappa_0 = 0.00571$ to $\kappa_1 = 1.005(1/H)$. The obtained time history of height, velocity, force, and gas density is shown in Figure 9*b*. At the early phase, the type B field line evolves almost in the same way as the type A field line; however, at the late phase ($60 < t < 100$) the upward velocity significantly decreases and the height of the field line comes close to a marginal value. Mathematically speaking, such strong deceleration is caused by the fact that κ is larger than $1/H$, whereby both terms on the right-hand side of equation (24) become negative. This causes a strong downflow in the middle of the field line, which starts to shrink toward the surface (at this stage the average velocity given by eq. [27] is no longer valid). However, physically speaking, such a strong downflow locally compresses the magnetic field and decreases a scale height, H. When $1/H$ becomes larger than κ, the downflow is decelerated and eventually the field line may come to a less dynamical state. Since the time history of force shows that the magnetic pressure force and magnetic tension force are almost comparable in size at the late phase, we expect that the type B field line could reach force-free equilibrium with a certain height. On the other hand, the gravitational force becomes much weaker than those two forces because plasma drains efficiently under the effect of increasing curvature.

For the type C field line, we use a time-dependent curvature given by

$$\kappa(t) = \kappa_0\left(1 - 0.875\frac{t}{100}\right), \quad (29)$$

where $\kappa_0 = 0.00571$. We also take the same H, v_{Ai}, and B_i that are taken for the type A and type B field lines. Compared to the type A field line, the type C field line shows similar evolution in Figure 9*c*, although the upward velocity decreases with time as the curvature decreases. This is because more plasma can remain in such a flatter field line as the type C field line, thereby reducing magnetic buoyancy (see the time history of gas density in Fig. 9*c*). Furthermore, as the field line becomes flatter, the magnetic tension force becomes less effective than the other two forces.

Among those three types of emerging field lines, the type A field line is the most dynamical and a group of these field lines form an outer layer of an emerging flux tube (see Fig. 4). They continue to expand widely in the corona while the footpoints of these field lines are confined to a small area at the photosphere. On the other hand, the type B and type C field lines represent inner field lines of an emerging flux tube. These field lines are almost aligned along the neutral line, and they connect opposite polarity regions with intense magnetic flux at the photosphere (see Fig. 2). Moreover, those two types of field lines are less dynamical in the corona than the type A field line. The type B field line has a vertically elongated shape and could reach force-free equilibrium, while the type C field line basically continues dynamic evolution; however, its speed is slow because magnetic buoyancy is ineffective in a horizontally stretched field line. The difference of dynamic evolution between the type B and type C field line leads us to expect that

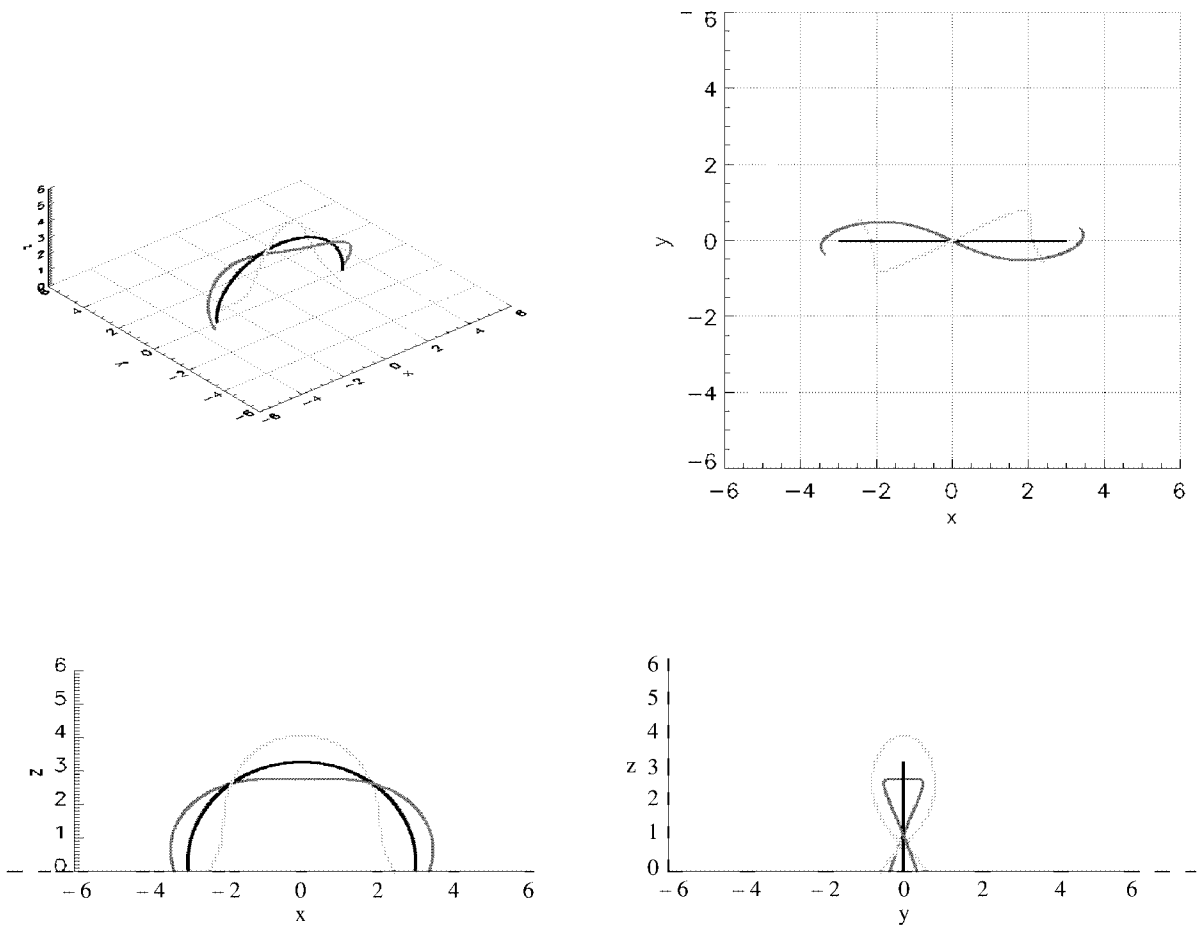

FIG. 10.—Four snapshots (top, side, front, perspective views) of three space curves in Cartesian coordinates (only $z > 0$ is shown). Light gray and dark gray curves lie on the surface of a torus, while a black curve lies on the common axis of these tori, which is circled by the light gray and dark gray curves in a left-handed way.

those two types of field lines form different quasi-static magnetic structure in the corona. The type B field line could form a less massive (and therefore high Alfvén velocity), quasi-static magnetic loop in which the magnetic pressure force is balanced against the magnetic tension force. If such magnetic loops are illuminated by some adequate heating process, they might be observed as coronal loops. On the other hand, the slowly evolving type C field line could form the magnetic structure for filaments and prominences, which includes long horizontal field lines above the neutral line. In this respect, it seems to be difficult to form long horizontal field lines simply by the emergence of a straight flux tube. This difficulty has been suggested by the two-dimensional simulations of an emerging flux tube presented in Magara (2001), which assumed translational invariance along the axis of an emerging flux tube and showed that the field line on the straight axis hardly emerges into the surface because plasma on this axis does not drain, thereby making magnetic buoyancy ineffective. In Figure 4 a sidelobe emerges at both sides of the central lobe and forms a new bipolar region at the photosphere, which will interact with emerging field lines in the central lobe. Thus, it is interesting to examine whether such interaction leads to forming long horizontal magnetic structure above the neutral line (Martens & Zwaan 2001). Finally, the dynamic character of the type C field line might play an important role in causing prominence eruptions and coronal mass ejections (Low 1996, 2001), although those topics are beyond the scope of the present study.

5. CHIRALITY OF EMERGING FIELD LINES

The chirality of coronal structure has been widely studied using solar observations. There are two types of filaments, known as dextral and sinistral (Martin & McAllister 1996, 1997). We also know that sigmoids, soft X-ray coronal loops observed in some active regions, have a forward S or backward S shape (Rust & Kumar 1996; Canfield, Hudson, & Pevtsov 2000). Furthermore, the relation between filament chirality and the chirality of interplanetary magnetic clouds has been investigated (Bothmer & Rust 1997).

Figure 10 shows three space curves in the Cartesian coordinates, a light gray and dark gray curve lying on the surface of a torus and a black curve lying on the common axis of these tori. The light gray and dark gray curves circle the axis in a left-handed way. The formula of those curves is given by

$$x = (R + r\cos u)\cos v,$$
$$y = R - r\sin u,$$
$$z = (R + r\cos u)\sin v - R\sin\left(\frac{\pi}{2} - \frac{l}{R}\right), \qquad (30)$$

where (u, v) are parameters while (R, l, r) are constants ($R = 3$, $l = 5$). For the black curve, $r = 0$. For the light gray curve, $r = 0.8$ and u is expressed as a function of v:

$$f(v) \equiv 0.75\pi\left(v - \frac{\pi}{2}\right). \qquad (31)$$

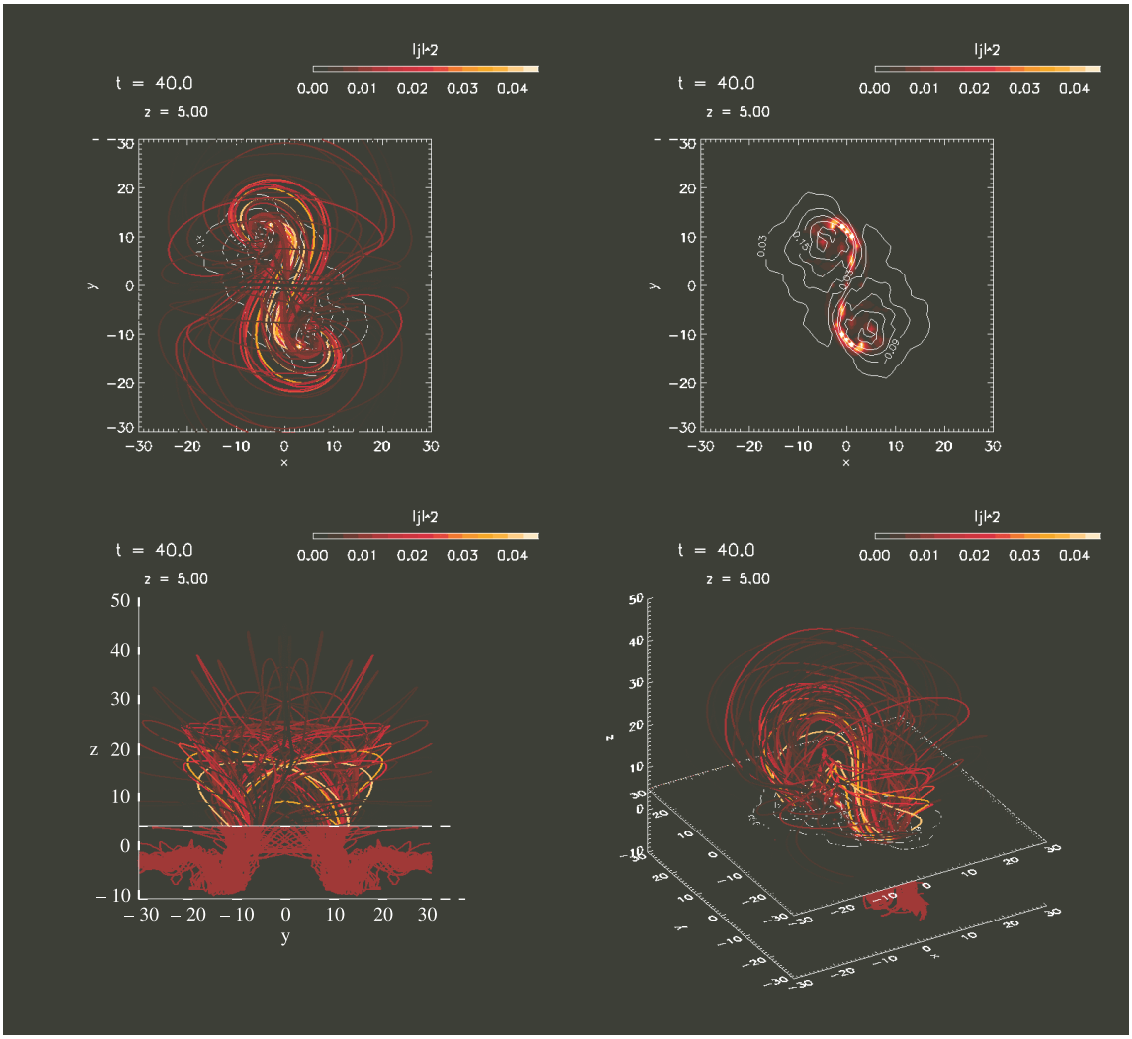

FIG. 11.—Snapshots of a modeled sigmoid. Colors of field lines represent the square value of current density at their footpoints on a chromospheric plane located at $z = 5$ (if the value at one footpoint is larger than the other, then the larger value is used to define the field line color). A horizontal color map represents the square value of current density at the chromospheric plane, and contours on this map show the vertical magnetic flux. Top view (*top left*), top view without field lines (*top right*), side view (*bottom left*), and perspective view (*bottom right*) are presented.

For the dark gray curve, $r = 0.5$ and u is given by

$$u = f(v) + \pi, \tag{32}$$

where $f(v)$ is defined in equation (31).

When we focus on the spatial relations of those curves, the light gray curve overlies the black curve and the dark gray curve underlies the black curve. Furthermore, the top view of those curves indicates that the light gray curve has a forward S shape and the dark gray curve has a backward S shape. When we use those curves as a model of emerging field lines that form a flux tube with a left-handed twist, the light and dark gray curves represent the outer and inner field lines, respectively. As we have discussed in the previous section, inner field lines are less dynamical than outer field lines, so inner field lines could form quasi-static magnetic structure in the corona. We therefore expect that such quasi-static structure assumes the shape of inner field lines, a backward S shape in this case. Similarly, an emerging flux tube with a right-handed twist could form quasi-static structure in a forward S shape.

We here examine the chirality of emerging field lines that are illuminated by some unknown heating process. Since we do not have a precise heating mechanism of coronal magnetic fields, we here refer to the distribution of current density at the footpoints of emerging field lines (Lee et al. 1998; Magara & Longcope 2001; Török & Kliem 2003). Nonzero current at those footpoints could be dissipated to provide a footpoint energy source for heating plasma distributed along the field line. Figure 11 displays the same field lines as in Figure 4, although the color of individual field lines reflects the square value of current density at their footpoints. The bright field lines in this figure clearly show backward S-shaped structure, indicating that the structure is formed by several sets of sigmoidal field lines (Gibson et al. 2002).

6. SUMMARY

In this paper we study the dynamic evolution of emerging field lines, focusing on how the shape of field lines affects their evolution. The following is a summary of the results:

1. Magnetic field lines at the outer and inner portion of an emerging flux tube expand into the atmosphere in a different way, which leads them into forming a different shape. Outer field lines spread out in a wide fan in the corona with a small

footpoint distance at the photosphere, while inner field lines tend to expand vertically without changing the footpoint distance dramatically.

2. Inner field lines are strongly confined by adjacent twisted field lines along the legs, which restricts the lateral expansion of inner field lines. On the other hand, outer field lines are almost free to expand without strong confinement by surrounding field lines.

3. We derive a simulation-based model that explains the dynamic evolution of emerging field lines. This model focuses on the plasma motion affected by a prescribed magnetic field, which is based on the fact that plasma motion is dominantly controlled by the magnetic field in such a magnetically strong region as the solar corona.

4. Using the simulation-based model, we find out that outer field lines tend to keep the same dynamical state, that is, they continue to expand in a widely spread fan shape. On the other hand, inner field lines are less dynamical than outer field lines and could form quasi-static magnetic structure in the corona. One case is that inner field lines reach force-free equilibrium when the curvature in the middle of a field line temporally increases. Another case is that inner field lines gradually reduce the rising speed as the curvature decreases. In the former case, inner field lines form a less massive magnetic loop in a vertically elongated shape, which might be observed as a coronal loop under some adequate heating process. In the latter case, inner field lines form a long, horizontally stretched magnetic loop filled with massive plasma. This slowly but still surely rising magnetic loop might provide a model of prominences and filaments whose dynamic aspect has recently been an important subject for theoretical modelings (Antiochos, MacNeice, & Spicer 2000; Karpen et al. 2001).

5. Since inner field lines more likely form quasi-static structure in the corona than outer field lines, the shape of inner field lines could appear as an observed property of coronal structure. We examine this using a model of sigmoid and find out that the shape of inner field lines rather than outer field lines is reflected in the chirality of sigmoid.

This work is financially supported by NASA ROSS-2000 NRA-00-01-SSS-057 and the Center for Integrated Space Weather Modeling (CISM; ATM-0120950). The numerical simulation has been performed with the assistance of the National Institute of Fusion Science in Japan.

APPENDIX

ANALYSIS OF THE EVOLUTION EQUATION

We here present a quantitative analysis of equation (24). For simplicity, we assume that κ is constant ($\kappa = \kappa_0$). In this case, equation (24) is written by

$$\ddot{Z}(t) = g_0 \left\{ \exp\left[-2\frac{Z(t)}{H} + \sqrt{g_0\kappa_0}\, t \right] - 1 \right\}, \tag{A1}$$

where we used equation (25) to eliminate v_{Ai}. Next, we define $q(t)$ to express the exponent on the right-hand side of equation (A1):

$$q(t) = -2\frac{Z(t)}{H} + \sqrt{g_0\kappa_0}\, t. \tag{A2}$$

If we differentiate equation (A2) twice with respect to t, we obtain

$$\ddot{q}(t) = -2\frac{\ddot{Z}(t)}{H}. \tag{A3}$$

We then replace $Z(t)$ by $q(t)$ in equation (A1) using equations (A2) and (A3). The result is

$$\ddot{q}(t) = -\frac{2g_0}{H}\left(e^{q(t)} - 1 \right). \tag{A4}$$

The initial condition of equation (A4) is given by

$$q(0) = -2\frac{Z(0)}{H} = 0 \tag{A5}$$

and

$$\dot{q}(0) = -2\frac{\dot{Z}(0)}{H} + \sqrt{g_0\kappa_0} = \sqrt{g_0\kappa_0}. \tag{A6}$$

Since the right-hand side of equation (A4) works as the conservative force for motion, the solution satisfying the initial condition given by equations (A5) and (A6) might be given by

$$\int_0^t dt' = \int_0^q \frac{dq'}{\left[g_0\kappa_0 + (4g_0/H)(1 + q' - e^{q'}) \right]^{1/2}}. \tag{A7}$$

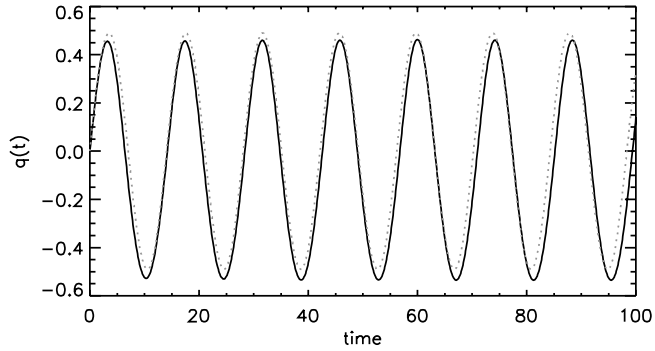

FIG. 12.—Temporal development of $q(t)$ in the case of $H = 12$ and $\kappa_0 = 0.04$. A solid line shows the solution obtained by integrating eq. (A4), and a dotted line represents an approximate solution given by eq. (A9).

Now we return to equation (A4) and take the Taylor expansion of the exponential term on the right-hand side. When we take the first order of expansion, equation (A4) is approximately written by

$$\ddot{q}(t) \sim -\frac{2g_0}{H} q(t). \tag{A8}$$

Then we solve equation (A8) under the initial condition given by equations (A5) and (A6). The result is

$$q(t) = \frac{\sqrt{g_0\kappa_0}}{\omega} \sin \omega t, \tag{A9}$$

where $\omega = (2g_0/H)^{1/2}$. As we have shown in § 4.2, the initial force balance requires $\kappa_0 H < 1$, which is equivalent to

$$\frac{\sqrt{g_0\kappa_0}}{\omega} < \frac{1}{\sqrt{2}}. \tag{A10}$$

In this case equation (A9) shows that $|q| < 1$ is satisfied for the Taylor expansion. Substituting equation (A9) into equation (A2) and differentiating this once with respect to t, we obtain an expression of $\dot{Z}(t)$:

$$\dot{Z}(t) = \frac{H}{2}\sqrt{g_0\kappa_0}(1 - \cos \omega t). \tag{A11}$$

Equation (A11) indicates that $\dot{Z}(t)$ oscillates within the positive range and its period and average velocity are given by equations (26) and (27), respectively. In Figure 12 we compare equation (A9) with the solution obtained by numerically integrating equation (A4).

REFERENCES

Abbett, W. P., & Fisher, G. H. 2003, ApJ, 582, 475
Antiochos, S. K., MacNeice, P. J., & Spicer, D. S. 2000, ApJ, 536, 494
Bothmer, V., & Rust, D. M. 1997, in Coronal Mass Ejections, ed. N. Crooker, J. A. Joselyn, & J. Feynman (Geophys. Monogr. 99; Washington, DC: AGU), 139
Canfield, R. C., Hudson, H. S., & Pevtsov, A. A. 2000, IEEE Trans. Plasma Sci., 28, 1786
Fan, Y. 2001, ApJ, 554, L111
Fan, Y., & Gibson, S. E. 2003, ApJ, 589, L105
Gibson, S. E., et al. 2002, ApJ, 574, 1021
Karpen, J. T., Antiochos, S. K., Hohensee, M., & Klimchuk, J. A. 2001, ApJ, 553, L85
Krall, J., Chen, J., Santoro, R., Spicer, D. S., Zalesak, S. T., & Cargill, P. J. 1998, ApJ, 500, 992
Lee, J., McClymont, A. N., Mikic, Z., White, S. M., & Kundu, M. R. 1998, ApJ, 501, 853
Low, B. C. 1996, Sol. Phys., 167, 217
———. 2001, J. Geophys. Res., 106, 25141
Magara, T. 1998, Ph.D. thesis, Univ. Kyoto
———. 2001, ApJ, 549, 608
Magara, T., & Longcope, D. W. 2001, ApJ, 559, L55
Magara, T., & Longcope, D. W. 2003, ApJ, 586, 630 (Paper I)
Martens, P. C., & Zwaan, C. 2001, ApJ, 558, 872
Martin, S. F., & McAllister, A. H. 1996, in Magnetohydrodynamic Phenomena in the Solar Atmosphere, Prototypes of Stellar Magnetic Activities, ed. Y. Uchida, H. S. Hudson, & T. Kosugi (Dordrecht: Kluwer), 497
———. 1997, in Coronal Mass Ejections, ed. N. Crooker, J. A. Joselyn, & J. Feynman (Geophys. Monogr. 99; Washington, DC: AGU), 127
Matsumoto, R., Tajima, T., Chou, W., Okubo, A., & Shibata, K. 1998, ApJ, 493, L43
Matsumoto, R., Tajima, T., Shibata, K., & Kaisig, M. 1993, ApJ, 414, 357
Nozawa, S., et al. 1992, ApJS, 78, 267
Parker, E. N. 1955, ApJ, 121, 491
Rust, D. M., & Kumar, A. 1996, ApJ, 464, L199
Shibata, K., Tajima, T., & Matsumoto, R. 1990, Phys. Fluids B, 2, 1989
Shibata, K., Tajima, T., Steinolfson, R. S., & Matsumoto, R. 1989, ApJ, 345, 584
Tajima, T., & Shibata, K. 1997, Plasma Astrophysics (Massachusetts: Addison-Wesley)
Török, T., & Kliem, B. 2003, A&A, 406, 1043
Yokoyama, T., & Shibata, K. 1996, PASJ, 48, 353